CHAPTER III
RESEARCH METHODOLOGY

The research methodology is divided into three sections. The first section covers computer simulations performed in CST Studio Suite, detailing each step of the simulation process. The second section addresses the design and placement of vacuum components, including leak checking of the vacuum chamber to ensure operational readiness and positioning the power supplies beneath the beamline to achieve a compact system layout. The third section presents the development and design of the ionizer heater.

3.1 Simulation using CST Studio Suite

This section presents the computer simulations carried out with CST Studio Suite. Simple 3D geometries were generated directly in CST, while more complex 3D models were created in SolidWorks by an engineer from NARIT.

3.1.1 Particle tracking simulation

In the CST workflow, the Particle Tracking Solver module is used. It is essential to select an appropriate mesh type and sufficient mesh density to ensure that simulation results are both reliable and accurate, while avoiding unnecessary consumption of computational resources. The flow chart of the simulation process is shown in Figure 3.1.

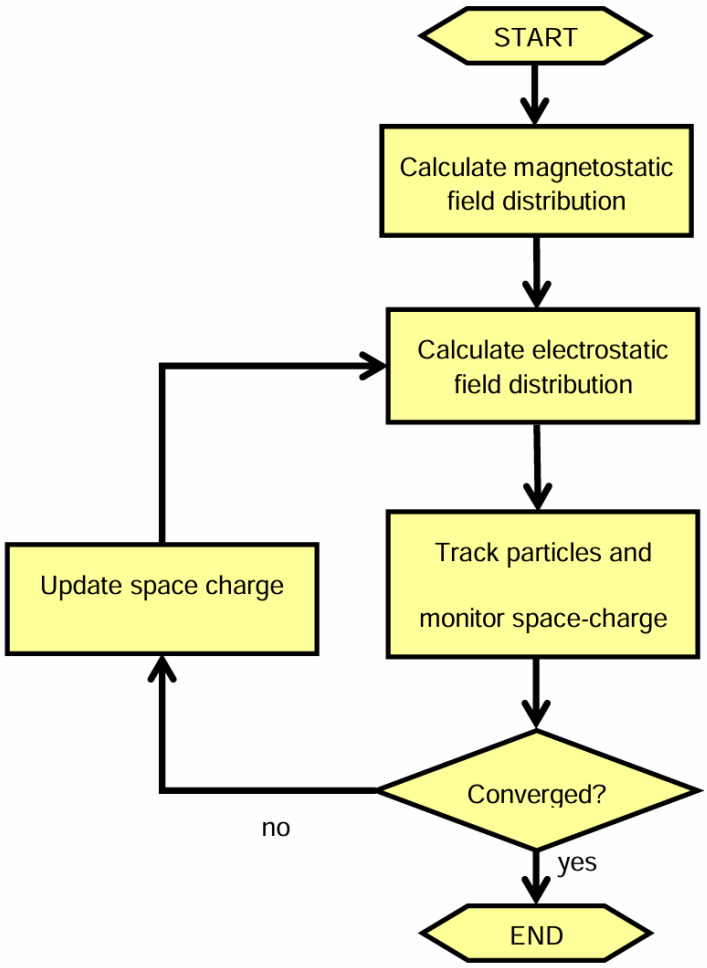

Figure 3.1 Flow chart of particle tracking simulation in CST Studio Suite.

3.1.1.1 Mesh refinement

In the Particle Tracking Solver module, a hexahedral mesh (brick cells) is employed to track particle trajectories through the electric fields computed from Maxwell's equations. Local mesh refinement is applied, as shown in Figure 3.2, along the ion beam path and in regions with high field gradients—such as around the emission surface and at electrode edges—to increase mesh density where it is most critical. A convergence study is then conducted to determine the optimal cell size. This strategy ensures that accurate particle tracking results are achieved while minimizing the use of computational resources.

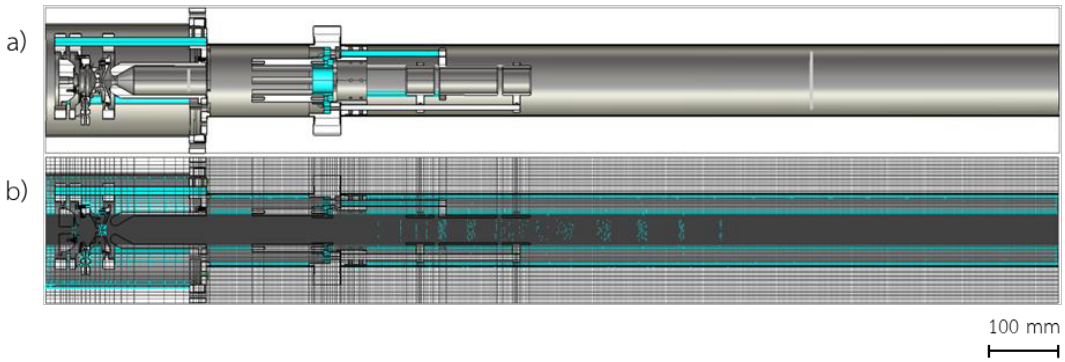

Figure 3.2 Mesh Generation for the particle tracking solver module in CST Studio Suite. a) The negative carbon ion beamline model used for simulation. b) The same model after applying local hexahedral mesh refinement along the ion beam path, from the ion source to the aperture slit at the end of the beamline.

3.1.1.2 Convergence study

In the simulation workflow, a convergence study was conducted to ensure that key beam parameters, such as emittance and the beam envelope, remained invariant with respect to increasing mesh density. Starting from a baseline hexahedral mesh size, the global mesh was systematically refined by varying the parameter *N_mesh*, as shown in Figure 3.3, which represents the number of cells per maximum model box edge.

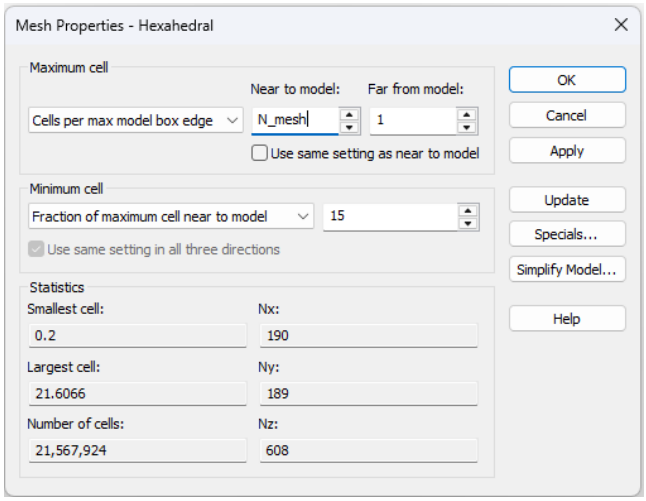

Figure 3.3 The global mesh settings, where the N_mesh variable is defined in the mesh properties, are used with the parameter-sweep function to perform the convergence study.

The convergence study was initiated with N_mesh = 20 and incremented by 20 up to 200, as shown in Figure 3.4, with local refinements introduced around high-gradient regions and along the ion beam path. At each refinement step, a parameter-sweep function was employed to iteratively increase N_mesh and to position particle monitors along the beam axis.

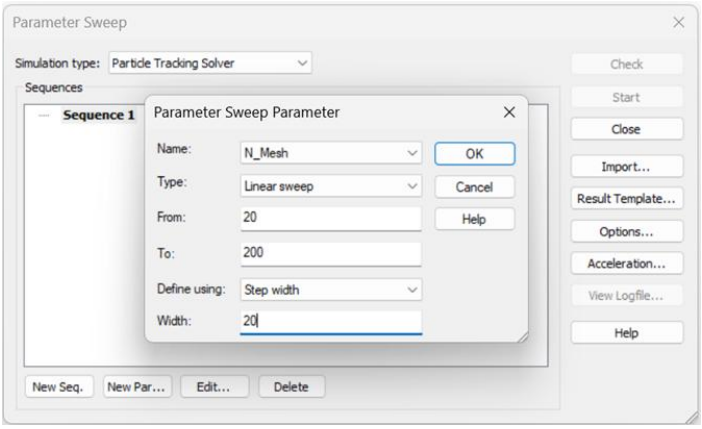

Figure 3.4 In the parameter sweep function, the N_mesh variable is swept from 20 to 200 in steps of 20, yielding 10 values (20, 40, 60, ..., 200) and progressively increasing the mesh density.

The Particle Tracking Solver was then executed, and the beam parameters were recorded. Convergence was considered achieved when successive refinements resulted in changes of less than 1 % in all monitored parameters. This threshold is widely accepted in fields employing Field/PIC/FEM techniques, as it represents a practical balance between high accuracy and manageable computational cost. This process not only ensures that the results are free from artifacts caused by mesh coarseness or insufficient particle sampling but also identifies the optimal balance between computational efficiency and accuracy, thereby enhancing both the reliability and effectiveness of the simulation methodology.

3.1.1.3 Transfer source via define particle export interface

In the simulation of the negative carbon ion beamline, multiple sequential components—ion source, octupole deflector, Einzel lens, and aperture slit—are modeled. To conserve computational resources and reduce simulation time, the particle export interface (shown in Figure 3.5) is employed to transfer the output of one optical element as the input source for the next.

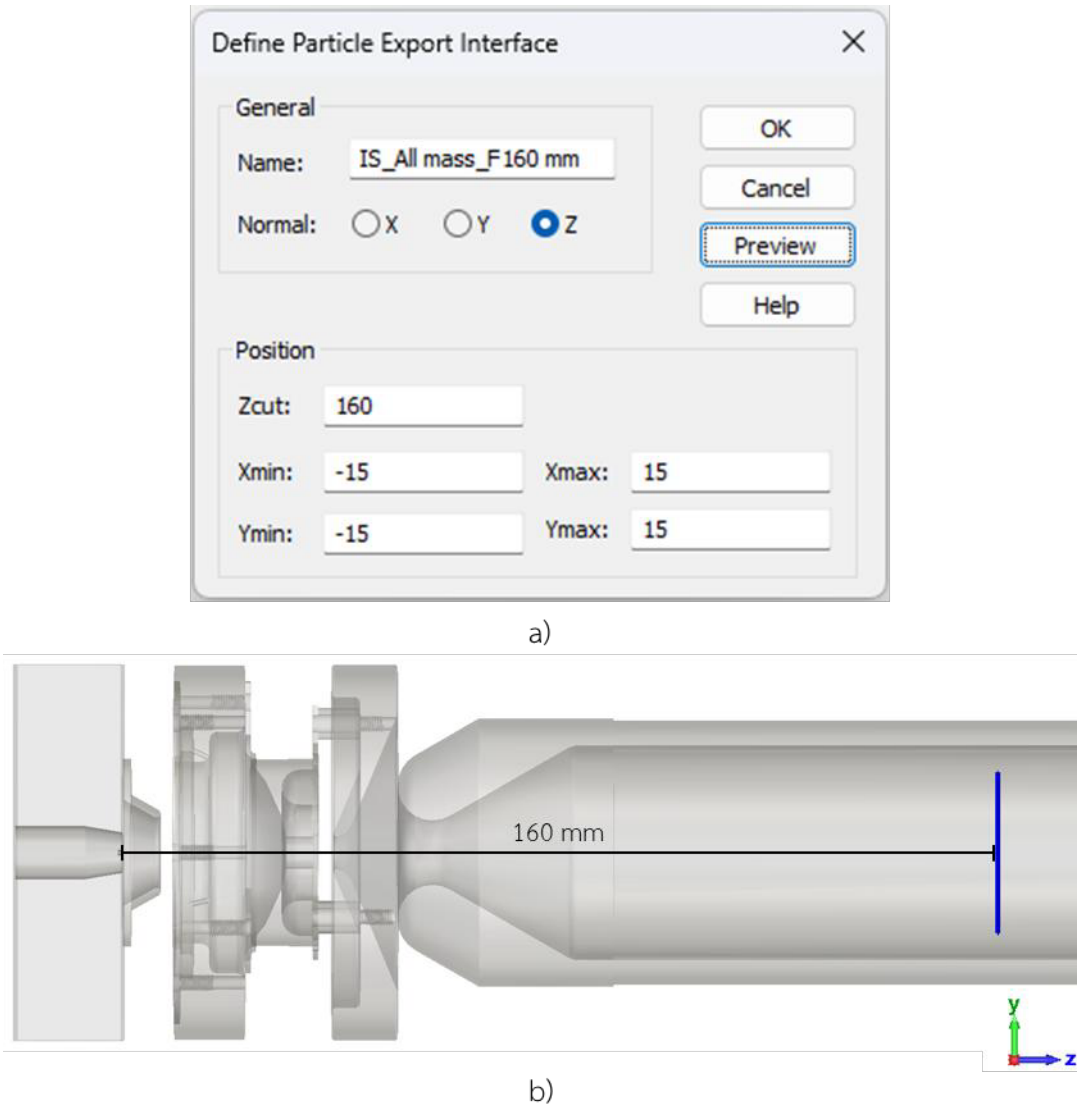

Figure 3.5 Defining the particle export interface. a) Boundary and position setup for particle export at the ion focus point, located 160 mm from the emission point; the boundary plane is sized larger than the beam envelope. b) Example of the particle export interface (blue plane) defined for the ion source, using the known focal position of the ion beam.

Specifically, the particle interface is exported at the focal point of the first element (e.g., the ion source) and then imported as the starting beam for the subsequent element (octupole deflector, followed by the Einzel lens, etc.). This chaining approach ensures an efficient and accurate end-to-end beamline simulation.

3.1.2 Ion source simulation

Since Saengwises et al. (2024) have already optimized the ion source model for a cesium-sputter AMS source, our simulation defines a particle source comprising ^{12}C, ^{13}C, and ^{14}C ions. Each ion carries a charge of -1.6×10^{-19} C and has a mass of 12 amu, 13 amu, and 14 amu, respectively, for a total of 118,803 particles. This particle count corresponds to the emission density specified in CST.

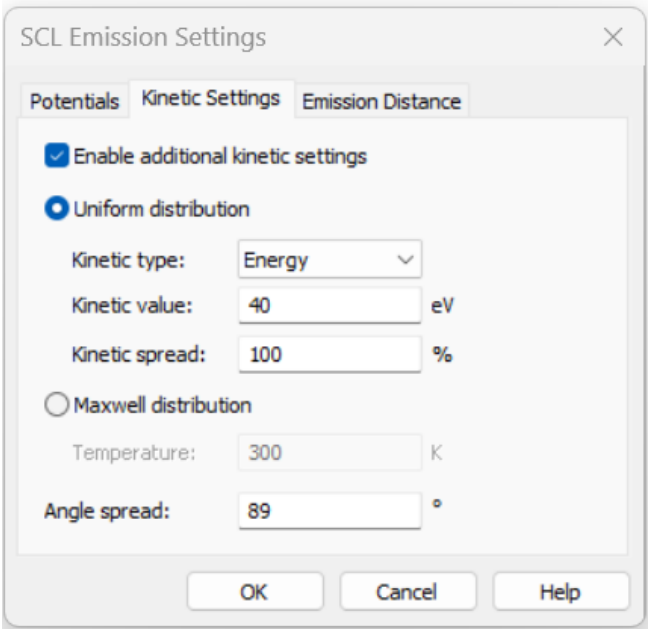

Figure 3.6 Setting the kinetic energy and angular spread of the particle sources to model the effects of HVPS ripple and the sputtering process respectively.

The requirement for generating the necessary electric field inside the ion source was addressed by applying a 40 kV potential difference using a high-voltage power supply (HVPS). Consideration was also given to the ripple, defined as the residual fluctuations on the DC output caused by imperfect filtering in the power circuit (Matsusada Precision Inc., 2023). The selected HVPS for the ion source exhibits a ripple of less than 0.1 % peak-to-peak. In CST, this required setting the source's kinetic energy spread to 40 eV (as shown in Figure 3.6) and defining an angular spread for the particle source to simulate the sputtering process, which emits negative carbon ions in all directions from the sample target. Due to CST's limitation in modeling a full 90° spread, the angular spread was set to 89°.

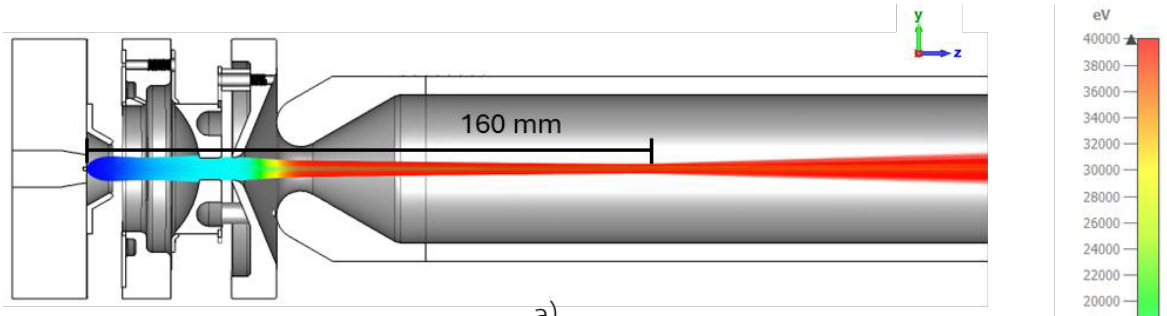

a)

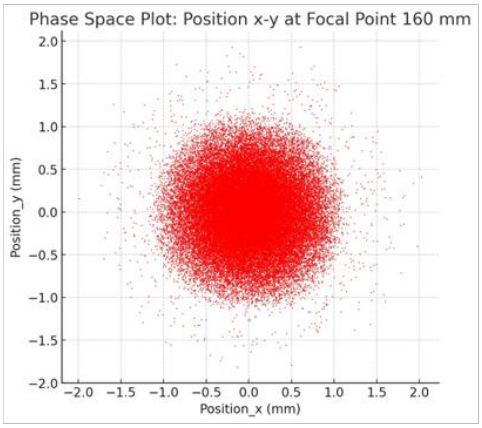

b)

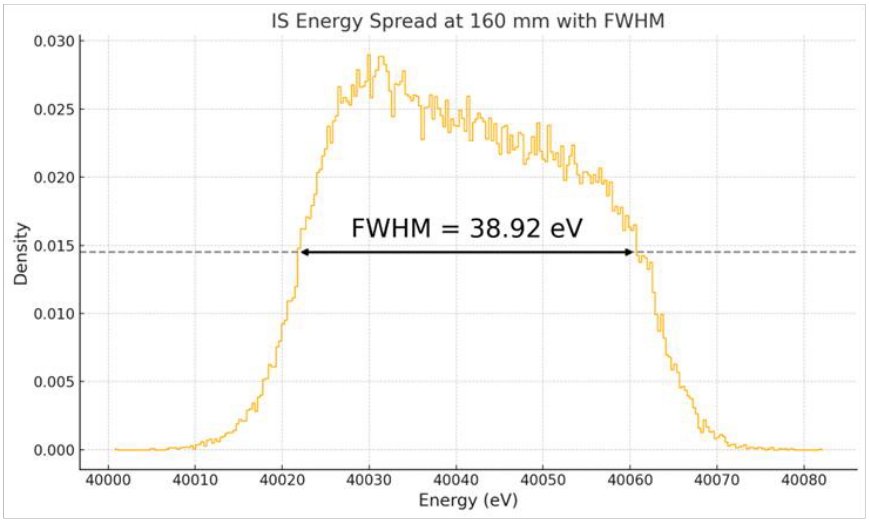

c)

Figure 3.7 Simulation results of the ion source a) Trajectories of ^{12}C, ^{13}C, and ^{14}C ions focused at 160 mm from the source. b) Particle distribution image at the focal point. c) Energy spreads at the focal point.

The simulation of the ion source, as shown in Figure 3.7, yielded 68,442 ions exiting the source, corresponding to a 58 % transmission. The 89° angular spread produces a larger beam that collides with the ionizer, causing particle loss. This is consistent with the actual ionizer wear marks shown in Figure 3.8. At the focal point, 160 mm from the source, the beam emittance was calculated to be 3.5 mm·mrad.

Figure 3.8 Comparison of a new ionizer (left) and a used ionizer (right), showing burn marks at the center caused by sputtered ions spreading in all directions and striking the surface Ref. Purdue University Prime Lab. (n.d.). Ionizer.

3.1.3 The study of miss alignment of the octupole deflector

During the fabrication and assembly of the actual components, misalignments—such as tilt and offset of the electrodes along the optical axis (z-axis) following the ion source—are inevitable. To define acceptable assembly tolerances, these errors were simulated. Based on the capabilities of the available alignment tools, the maximum expected offset is 1 mm, and the maximum tilt angle is 2°. In the simulation shown in Figure 3.9, two parameters were varied: the tilt angle (θ) at 0°, 0.5°, 1°, 1.5°, and 2°, and the offset of the octupole deflector along the y-axis at 0, 0.5, 1, 1.5, and 2 mm. The

objective was to determine the maximum tilt and offset that still allow the ion beam to be correctly focused at the aperture slit.

The power supply chosen for operating the octupole deflector (Matsusada Precision Inc., 2023) delivers up to 1 kV to every other rod, with the remaining four rods held at ground potential.

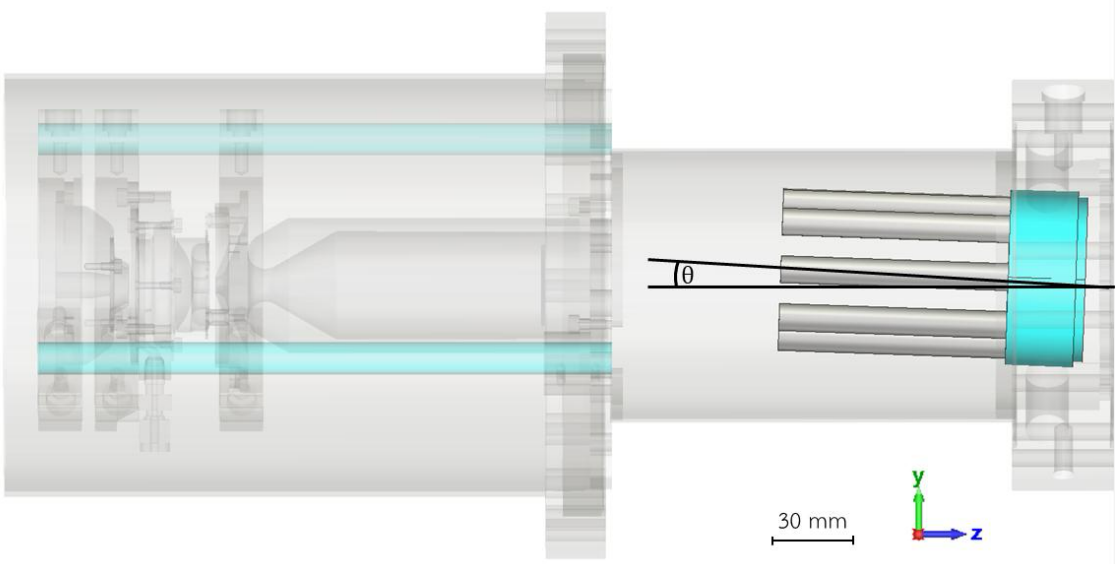

Figure 3.9 The octupole deflector model has rods each 10 mm in diameter and a total inner diameter of 40 mm, matching the dimensions from Figure 2.5 (Chomchan et al., 2024). This model was used to study tilt angles (θ) of 0°, 0.5°, 1°, 1.5°, and 2°, and offsets achieved by translating the entire octupole component along the positive y-axis by 0, 0.5, 1, 1.5, and 2 mm. The insulator segment is shown in blue.

In the simulation, two parameters—tilt angle and offset along the y-axis (offset_y)—were varied across five values each, resulting in a total of 25 parameter combinations. For each case, the particle monitor image placed at the aperture slit was examined to determine whether the beam remained focused and successfully passed through the slit. The aperture slit consists of four blades, each independently adjustable along the ±x and ±y axes. These blades can be fully opened to form a maximum square aperture of 20 × 20 mm² or closed completely, as shown in Figure 3.10.

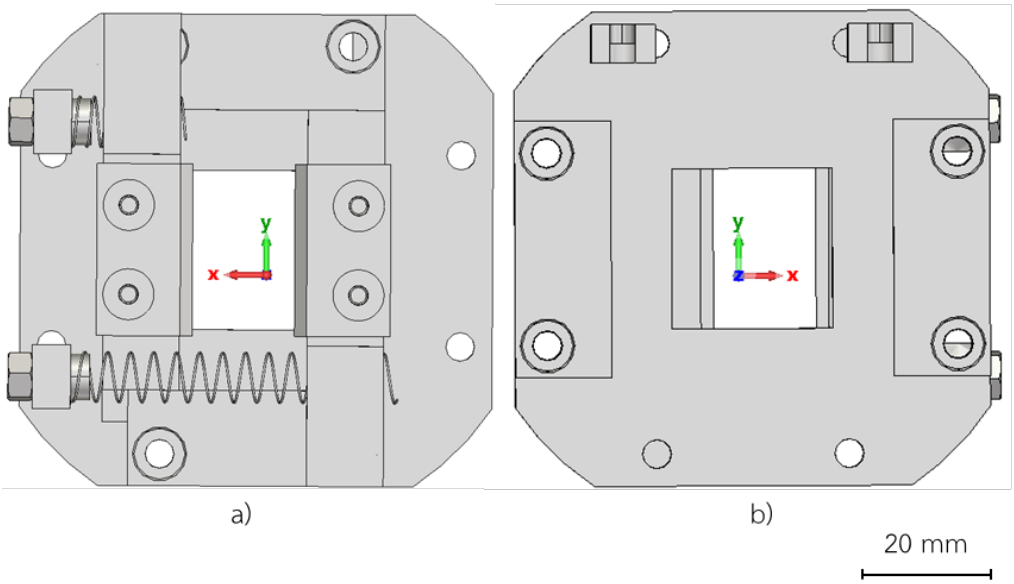

Figure 3.10 The aperture slit design consists of four independently adjustable blades, each movable along the ±x and ±y axes, allowing a maximum square opening of 20 × 20 mm^2 or complete closure. Each blade also serves as a current collector to measure and monitor the ion beam. a) Upstream side b) Downstream side.

3.1.4 Einzel lens simulation

The optical element downstream of the octupole deflector is an Einzel lens, which consists of three coaxial cylindrical electrodes with a 35 mm inner diameter and 3 mm wall thickness, as described by Suethonglang et al. (2024). The first and third electrodes are held at ground potential, while the central electrode is driven by a high-voltage power supply (Matsusada Precision Inc., 2023) providing a negative bias of up to 30 kV. The function of this Einzel lens is to focus the ion beam onto the aperture slit.

3.1.4.1 The study of effects from mounting support

The impact of the mounting supports on the ion beam was studied by including both the mounting support rods and the Einzel lens in the simulations. Although this approach increases computational resource usage and simulation time, it provides more accurate and realistic results. The Einzel lens consists of three coaxial cylinders with gaps between them, as shown in Figure 3.11.

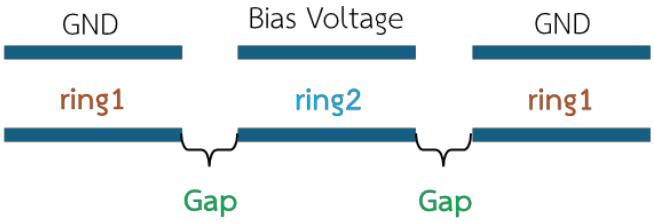

Figure 3.11 The ratio of the Einzel lens lengths (ring1 : gap : ring2).

Conductive stainless-steel support rods passing alongside the gaps between the electrodes can perturb the electric field and consequently affect the ion beam. To evaluate this effect, two models with different ring-to-gap ratios were analyzed. Model 1 employs a ratio of 43 : 21 : 64 mm (Figure 3.12), while Model 2 uses a ratio of 40 : 6 : 82 mm (Figure 3.13).

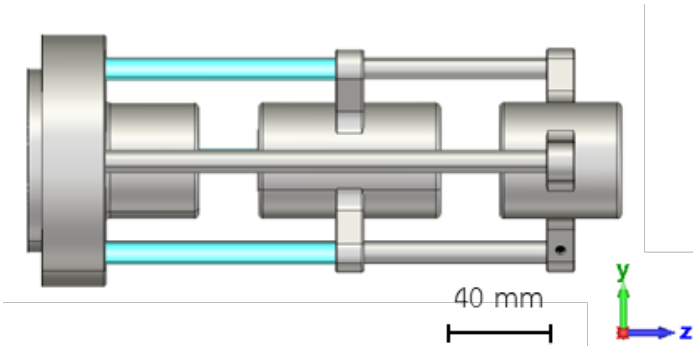

Figure 3.12 The Einzel lens model 1 (43 : 21 : 64 mm)

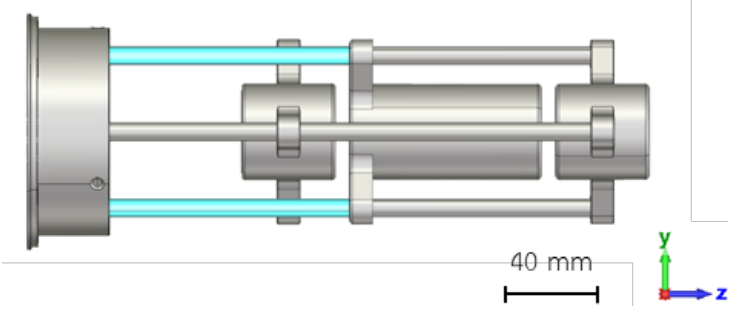

Figure 3.13 The Einzel lens model 2 (40 : 6 : 82 mm)

In the simulations, the particle source from the ion source was imported using the Particle Import Interface. The beam shape at the focal plane was then examined while a –20 kV bias was applied to the Einzel lens, and the electric field distribution near the support rods was observed.

3.1.4.2 The study of focal range

After the improved Einzel lens model was finalized, the optimizer function in CST was used to vary the applied potential to ensure that the ion beam focused at 476 mm from the Einzel lens—the position of the aperture slit. The optimization variable, *V_Einzel*, was defined as the bias voltage on the Einzel lens and was varied by the solver from 0 V to −30,000 V (Figure 3.14a). The optimization goal (Figure 3.14b) was to minimize *rms(position_x)* at the focal point, where *rms(position_x)* represents the root-mean-square of the particle positions.

a)

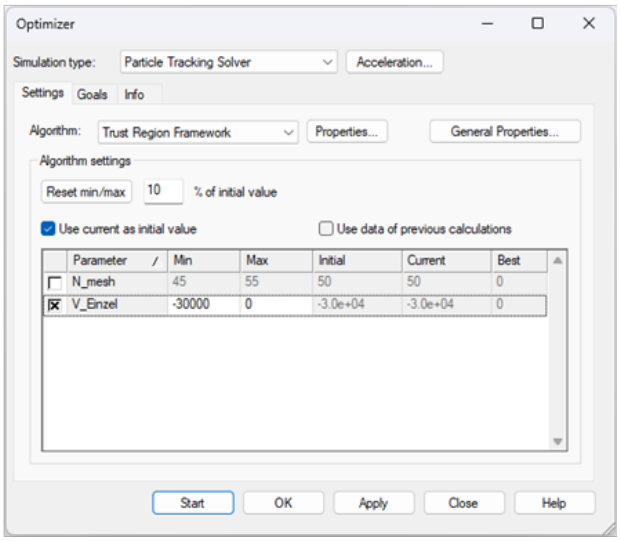

b)

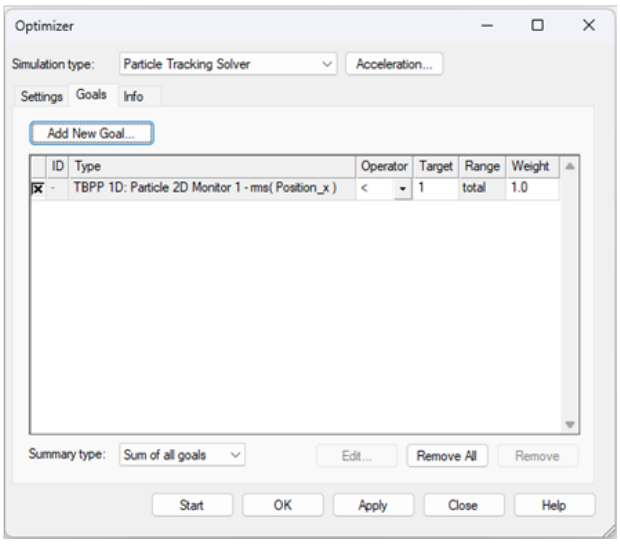

Figure 3.14 Optimizer Function Settings in CST Studio Suite a) Definition of variables and their ranges for the solver to vary. b) Specification of the optimization goals.

3.1.4.3 The study of miss alignment

When the actual components are fabricated and assembled, the Einzel lens aligned downstream of the octupole deflector shares mounting supports on a CF152 vacuum-chamber flange (shown as the leftmost electrode in Figure 3.15). During alignment, some degree of tilt or offset error is inevitable.

Simulations were therefore performed to specify the allowable assembly tolerances. Engineers defined the maximum expected alignment errors as a 1 mm offset and a 2° tilt. In the simulations (Figure 3.15), two parameters were varied: the tilt angle (θ) at 0°, 0.2°, 0.4°, 0.6°, 0.8°, 1.0°, 1.2°, 1.4°, and 1.6°, and the y-axis offset of the middle electrode by translating it 0, 0.2, 0.4, 0.6, 0.8, 1.0, 1.2, 1.4, and 1.6 mm along the positive y-axis. The focus was placed on the middle-ring electrode, as it is most susceptible to alignment errors due to its support rod being made of an alumina insulator (shown in Figure 3.12b, blue electrode), which is less rigid than the stainless-steel rods used for rings 1 and 3. For each parameter combination, the particle-monitor image at the aperture slit was examined to determine whether the beam remained focused on and successfully passed through the slit.

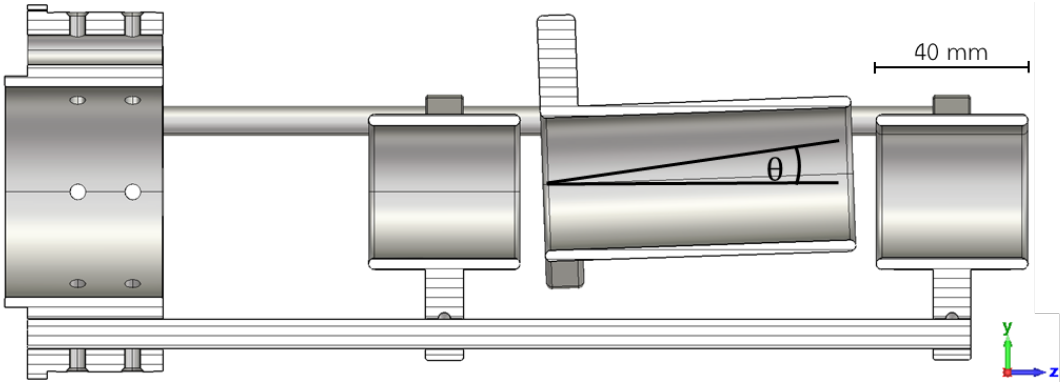

Figure 3.15 The cross section of Einzel lens design includes mounting supports (shown on the leftmost side) shared with the octupole deflector.

3.1.5 Low-energy negative carbon ion beamline simulation

In assembling the fully integrated system—which comprises the ion source, octupole deflector, Einzel lens, and aperture slit as primary components, along with various mounting supports inside the vacuum chamber—the CST model is simplified by omitting nonessential details such as vacuum pumps, chamber fittings, screws, and other hardware, as shown in Figure 3.16a. This simplification reduces computational load and simulation time. The model is then focused on the ion beam path and only those support structures likely to perturb the electric field (Figure 3.16b). Before initiating the simulation, the mesh is defined and a convergence study is performed to determine the optimal mesh density.

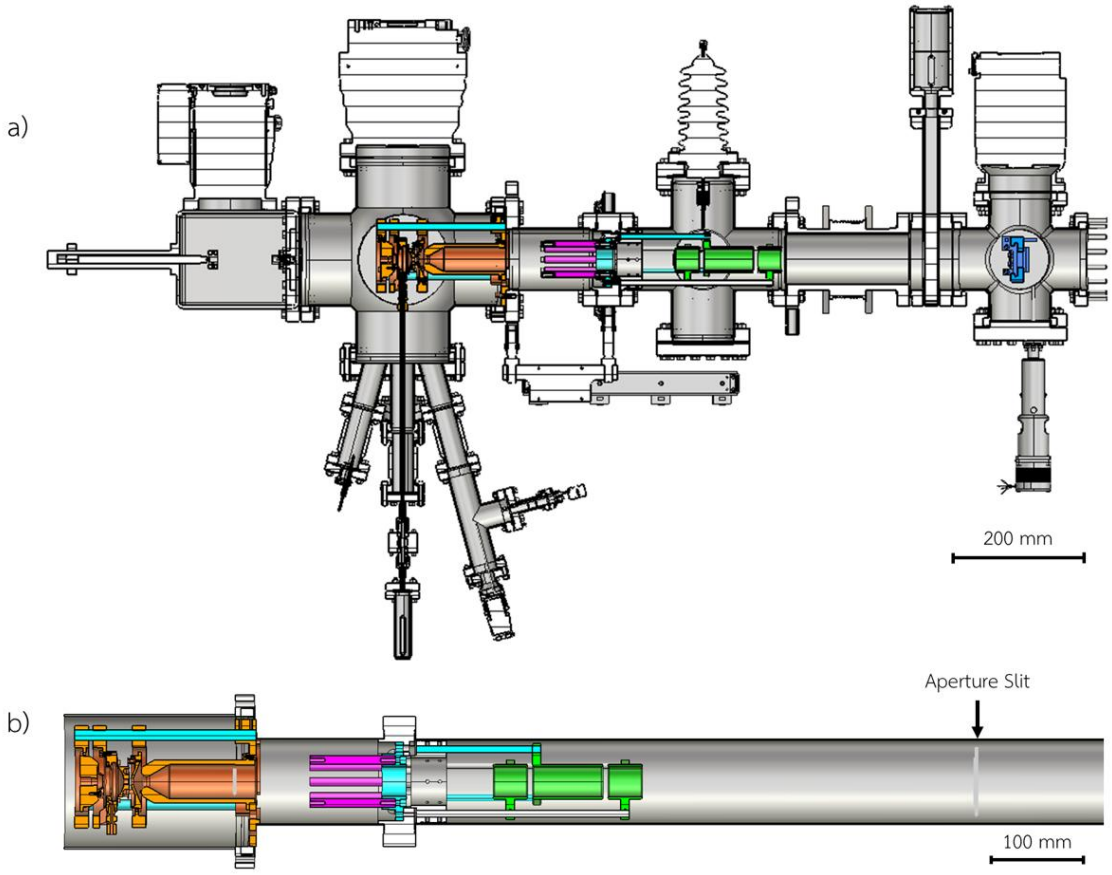

Figure 3.16 The cross-section of the low-energy negative carbon ion beamline shows the details and positions of the main components: the ion source (orange), the octupole deflector (pink), the Einzel lens (green), and the aperture slit (blue). The insulator segment is also highlighted. a) Beamline with external details. b) Simplified beamline model for particle-tracking simulation in CST.

In simulating the full system, the source was first defined using the Particle Import Interface to transfer the particle distribution at the ion source focus to subsequent stages, thereby reducing simulation time. The optimized bias voltage was then applied to the Einzel lens by setting V_Einzel to -2.01×10^4 volts, as determined from the focal-range study. This simulation represents an ideal case with perfect, systematic alignment. The beam size and emittance were examined along the entire optical axis and at the aperture slit using the Particle 2D Monitor function. Specifically, Monitor 1 was placed at the aperture slit, and 100 additional monitors (Monitor 2) were distributed from the ion source focal point through and slightly beyond the slit, as shown in Figure 3.17a. Post-processing was subsequently employed to analyze rms(position), beam envelope, beam image, and emittance, as illustrated in Figure 3.17b.

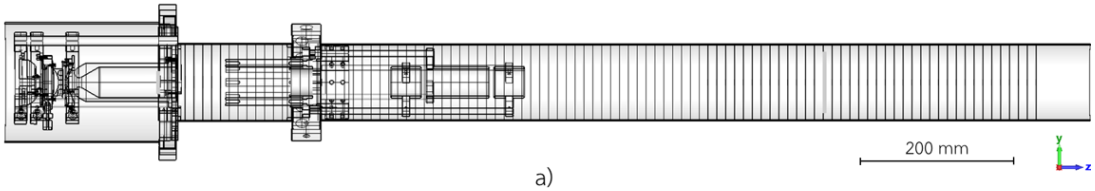

a)

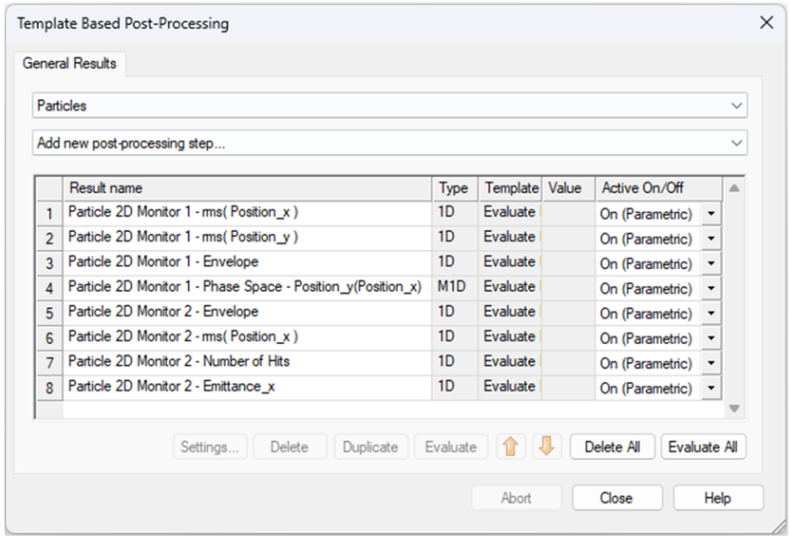

b)

Figure 3.17 Analysis of the ion beam using particle monitors. a) The 101 monitors spanning from the ion source focal point through and slightly beyond the aperture slit, including Monitor 1 at the slit and Monitor 2 along the beam path. b) Template based post processing showing the results as the ion beam passes each monitor.

3.2 Low-energy beamline design

For the operation of the AMS, the system must function under vacuum conditions. The vacuum system maintains an ultra-high vacuum environment, typically in the range of 10^{-6} to 10^{-9} Torr, which is essential for minimizing collisions between ions and residual gas molecules. To reduce procurement and manufacturing costs, existing vacuum components from SLRI's unused equipment inventory were selected, inspected, and prepared for vacuum operation before being assembled into the system layout. Assembly drawings were created in SolidWorks through collaboration with engineers from NARIT. For beamline sections requiring high-voltage operation, power supplies from Matsusada Precision Inc. were selected to match the specifications of each component. Finally, the power supplies were positioned beneath the beamline to achieve a compact system design.

3.2.1 Vacuum system

3.2.1.1 Existing vacuum components at SLRI

- 6-Ways Cross Chamber, 8" OD, Sphere Body 9" for ion source chamber

Figure 3.18 6-Ways Cross Chamber, 8" OD, Sphere Body 9 inch.

- Adapter CF203 to CF152 for octupole deflector

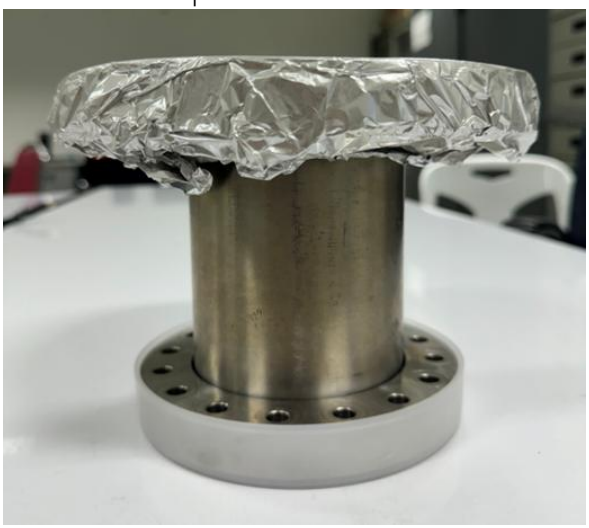

Figure 3.19 Adapter CF203 to CF152.

- 6-Ways Cross Chamber, 6” OD size 270 mm for Einzel lens

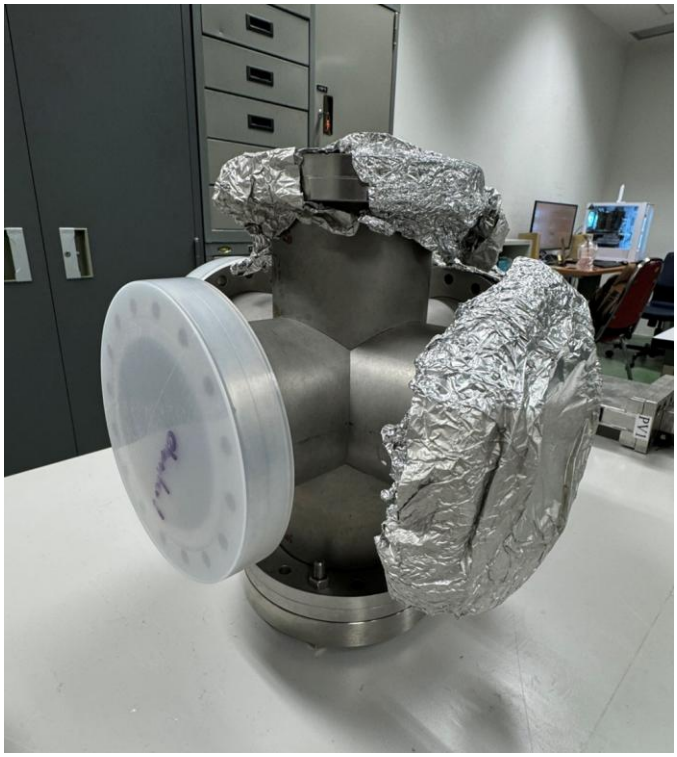

Figure 3.20 6-Ways Cross Chamber, 6” OD size 270 mm

- 6-Ways Cross Chamber, 6” OD size 220 mm for aperture slit.

Figure 3.21 6-Ways Cross Chamber, 6” OD size 220 mm

- Edge Weld Bellow CF152 and alignment studs for vacuum chamber extension.

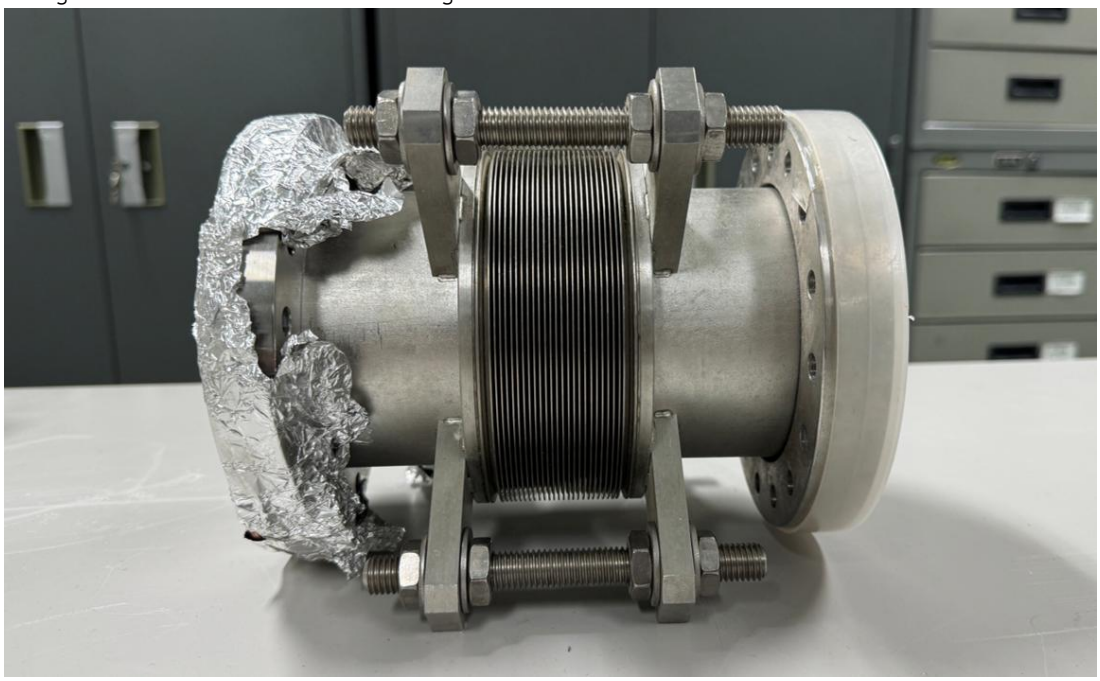

Figure 3.22 Edge weld bellow and alignment studs.

- Vacuum Gate Valve (CF152) for isolating vacuum sections

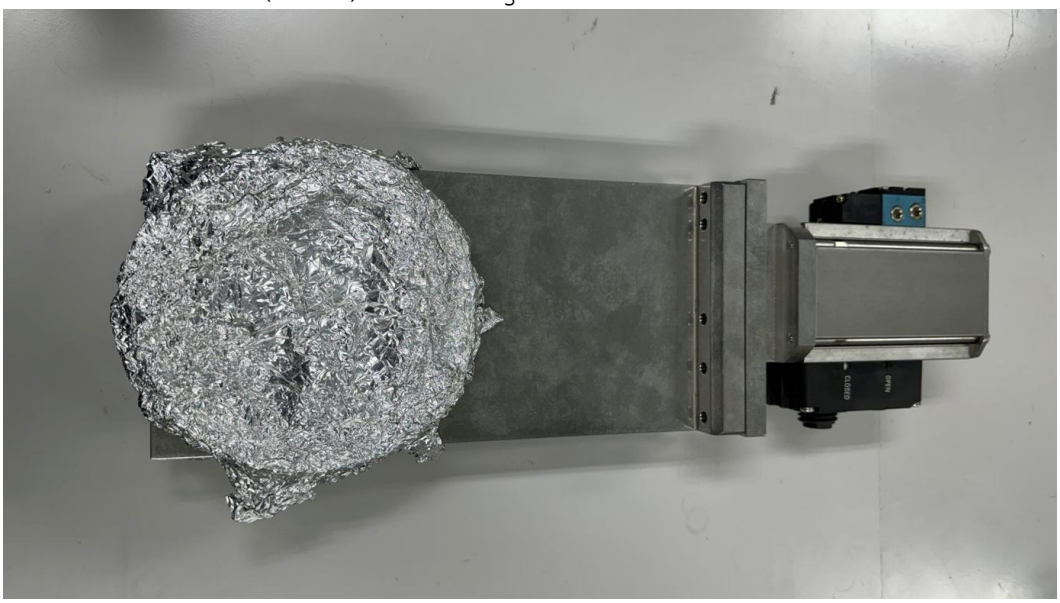

Figure 3.23 Vacuum gate valve

- Glass view port CF34, CF70, CF114 and CF152

Figure 3.24 Glass view port

3.2.1.2 Leak checking by helium detector

To prepare the vacuum chamber for operation, existing components from SLRI were cleaned, assembled, and tested for leaks. A Pfeiffer Adixen ASM 340 leak detector was used to verify vacuum integrity, and a reusable Viton gasket was chosen for sealing. Helium was applied to check for leaks, with a leak rate below 1×10^{-8} mbar·L/s indicating readiness for use.

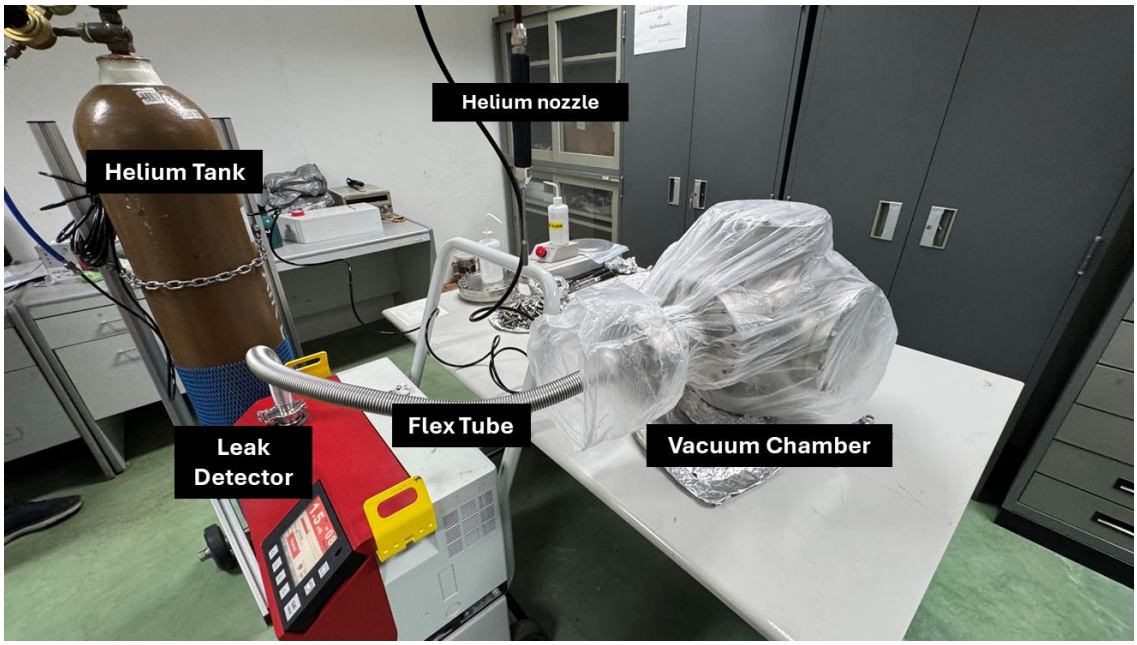

Figure 3.25 Setup of the leak-testing system using a Pfeiffer Adixen ASM 340 leak detector at SLRI.

Procedure:

- Cleaned all vacuum components with alcohol to remove contaminants.
- Assembled components and sealed the chamber using a reusable Viton gasket.
- Connected a Pfeiffer Adixen ASM 340 leak detector via a flexible hose.
- Activated the turbomolecular pump to evacuate the chamber.
- Applied helium around all seals and connections by spraying or enclosing them in a plastic bag.
- Waited 30 minutes for stabilization.
- Monitored helium leak rate; confirmed leak-tight condition if below 1×10^{-8} mbar·L/s.

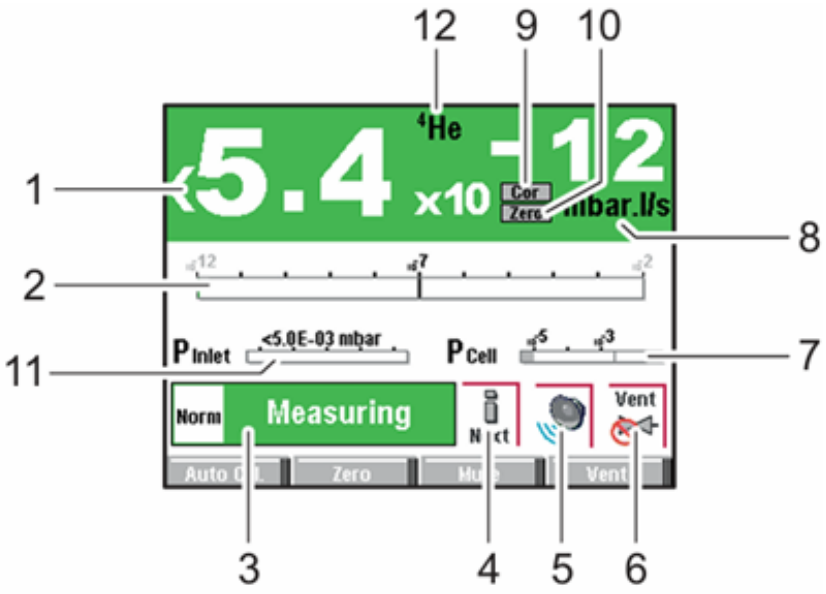

1	Digital display of the leak rate (green ≤ reject set point < red)
2	Bargraph display of the leak rate (adjustable scale)
3	Detector status and Detection mode
4	Access error information
5	Mute function indicator (except ASI 30)
6	Air inlet function indicator (except ASI 30)
7	Cell pressure bargraph display
8	Leak detector unit
9	Leak rate correction function indicator
10	Zero function indicator
11	Detector inlet pressure display (unit consistent with the leak rate unit)
12	Tracer gas (^{3}He, ^{4}He or H_2)

Figure 3.26 Monitoring and recording the leak rate and inlet pressure according to the operating instructions. Ref. Pfeiffer Vacuum GmbH. (n.d.). CF Vacuum Gate Valves [Product data sheet].

3.2.2 High Voltage Power Supply (HVPS)

A high-voltage power supply for mass spectrometry should provide stable DC output up to 60 kV with ultra-low ripple (≤0.001 % pp), tight voltage regulation (±0.01 %), and precise current control to avoid signal drift. It must include safety interlocks, remote control capability, and effective cooling (air or water) while fitting standard rack dimensions for laboratory integration (Matsusada Precision Inc., 2023).

3.2.2.1 HVPS for ion source

The internal components of the ion source designed for AMS require three distinct power-supply zones to generate the necessary electric fields, as illustrated in Figure 3.27. The first zone (green) includes the sample target, target support, and immersion lens, all operating at –40 kV. The second zone (orange) consists of the ionizer shroud, ionizer body, and ionizer support, with a voltage range of –35 kV to –28 kV to control the sputter energy during cesium sputtering. The third zone (blue) operates at ground potential.

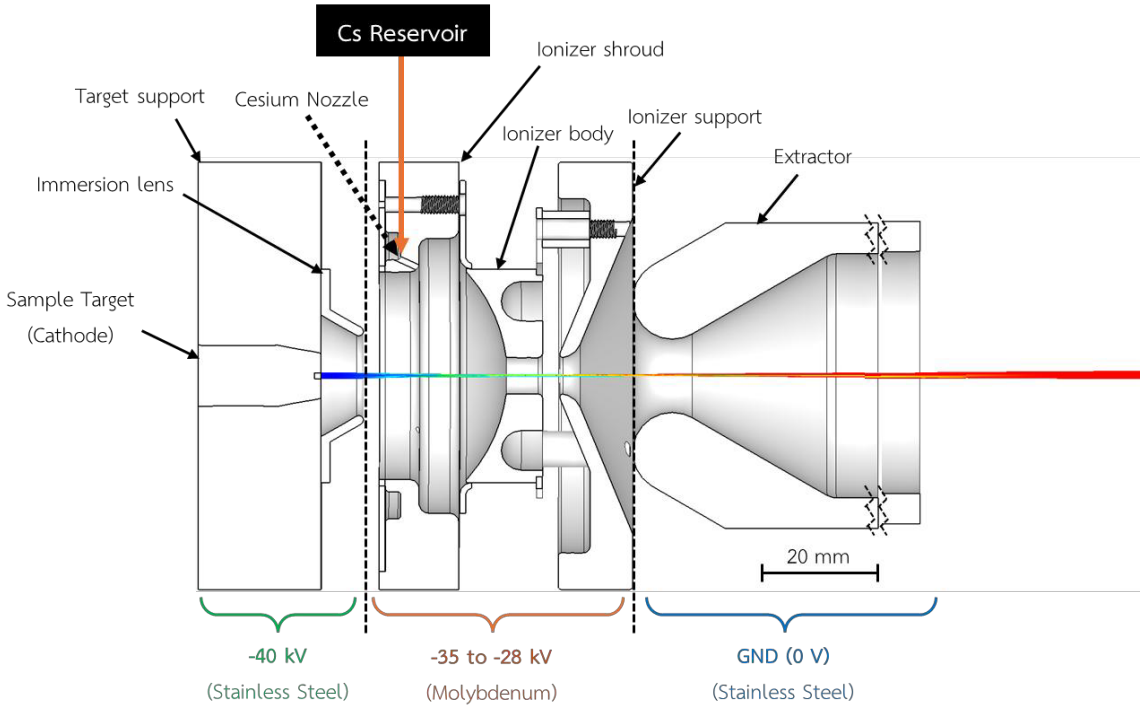

Figure 3.27 Simplified diagram of the power-supply zones for generating electric fields in the cesium sputter source for AMS at SLRI.

In addition to the electric fields, the cesium sputtering process requires three dedicated heaters. The first heater warms the cesium reservoir to about 120 °C so that liquid Cs vaporizes. The second heater maintains the vapor state in the cesium transport line, preventing condensation before the Cs nozzle. The third heater powers the MoRe filament located behind the ionizer body. According to Table 2.1, reaching a filament temperature of 1200 °C requires approximately 150 W of power.

3.2.2.2 HVPS for octupole deflector

The octupole deflector operates at a relatively low voltage and requires a stable, adjustable 1 kV DC supply to generate the internal electric field for beam steering. Figure 2.5 shows the schematic design of the deflector, which uses four independent rods. Each rod must be driven by its own power supply, so four identical 1 kV units are required to provide precise and independent voltage control.

3.2.2.3 HVPS for Einzel lens

Similarly, the Einzel lens requires a negative bias voltage on its central electrode to generate the focusing field, as shown in Figure 2.14. This bias is adjustable up to –30 kV and is supplied by a dedicated high-voltage unit to ensure stable and precise beam focusing.

3.2.2.4 High voltage isolation transformer

In operating the ion source, the three power supplies for the Cs reservoir, Cs line, and ionizer heater must float at the ionizer body potential of –30 kV. To reduce costs and avoid purchasing additional high-voltage power supplies, a high-voltage isolation transformer is used to float these supplies at –30 kV. Similarly, the graphite target requires –40 kV; by floating its supply on the same –30 kV reference, only a –10 kV power supply is needed to achieve the required –40 kV, further minimizing expenses. The isolation transformer must be mounted on an insulator or high-voltage bushing to ensure that the external beamline remains at ground potential.

3.2.3 Integrated system

By selecting existing vacuum components from SLRI and procuring the necessary power supplies, a low-energy negative carbon ion beamline for AMS was assembled based on the combined dimensions of these parts. Various component spacings were studied by creating detailed drawings in SolidWorks, followed by the production of a 3D-printed prototype of the system. This work was carried out in collaboration between SLRI and NARIT, with an emphasis on maintaining a compact design and ensuring that all external beamline structures remain at ground potential for safety.

3.3 The development of heater for ionizer

In the sputtering process within the ion source, the surface of the ionizer body plays a critical role in ionizing cesium vapor into Cs^+ ions. To enable this, the ionizer body surface must be heated to approximately 1200 °C. In the experiments, the heater coil positioned behind the ionizer body is tested. This coil, made from MoRe alloy, is wound in a toroidal shape. The required wire length and number of turns are calculated to ensure that the coil can achieve the necessary temperature.

3.3.1 Calculation and design of the toroidal heater

The AMS development project for radiocarbon dating at SLRI purchased MoRe filament wire with a 0.9 mm diameter, matching the specifications of the filament material used by HeatWave Labs Inc. (Figure 2.15). MoRe is an exceptionally strong alloy with a melting point around 2450 °C as shown in Table 2.2. The addition of rhenium increases its toughness and resistance to creep at high temperatures, preventing the wire from stretching or becoming brittle during operation. In vacuum, MoRe also exhibits lower metal evaporation than tungsten or graphite filaments, reducing chamber contamination and extending filament lifetime.

In calculating the required wire length, the electrical resistivity (ρ) is referenced from Figure 2.16, which shows that at an operating temperature of 1200 °C, ρ is 200 $\mu\Omega \cdot \mathrm{cm}$. Since resistivity increases with temperature, and Table 2.1 indicates a power requirement of approximately 150 W, the filament length needed for the toroidal heater can be determined using the following equations:

The electrical power equation is defined from the definitions of work W and electric current I. When calculating the power P :

$$\mathrm{P} = \frac{d\mathrm{W}}{dt} = \frac{d\mathrm{Q}}{dt}\,\mathrm{V} = \mathrm{IV} \qquad \text{Eq. 9}$$

Ohm's law describes by:

$$\mathrm{V} = \mathrm{IR} \qquad \text{Eq. 10}$$

Electrical resistance formula describes how the electrical resistance R of a uniform conductor depends on its material resistivity ρ, length L, and cross-sectional area A. It is given by the formula:

$$\mathrm{R} = \rho\frac{\mathrm{L}}{\mathrm{A}} \qquad \text{Eq. 11}$$

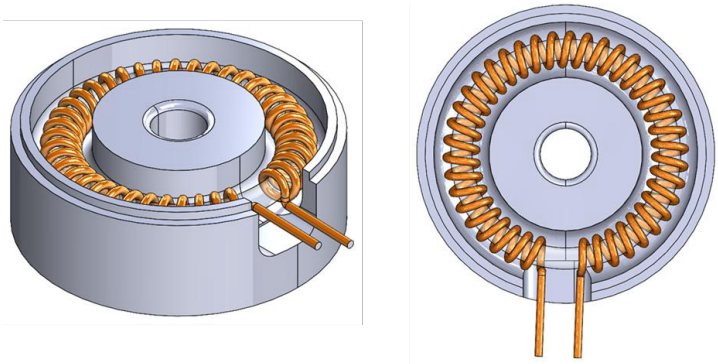

Figure 3.28 Toroidal heater with 40 turns installed inside the rear of the ionizer body.

At an operating temperature of 1200 °C, Table 2.1 indicates that the filament resistance, calculated using Ohm's law, is 0.6 Ω. Using the electrical resistance formula, the required wire length is determined to be approximately 0.2 m. Since the heater coil is mounted behind the ionizer body, an insulating material is required to prevent electrical shorting. Alumina (Al_2O_3) was selected to separate the coil from the ionizer body due to its excellent insulating properties. To achieve the target resistance, the coil must be wound with 22 turns around a 2 mm-diameter mandrel. However, during the creation of the SolidWorks drawing, it was found that doubling the number of turns is feasible. This modification increases the overall coil length, raises its resistance, and reduces power consumption, as illustrated in Figure 3.28.

The relationship between temperature and resistance in metals is typically described by the linear Temperature Coefficient of Resistance (TCR) equation, which is also known as the Resistivity Equation for Conductors.

$$R(T) = R_0[1 + \alpha(T - T_0)] \quad \text{Eq. 12}$$

Where:

- $R(T)$ is the resistance at temperature T,
- R_0 is the resistance at a reference temperature T_0 (often room temperature),
- α is the temperature coefficient of resistance (TCR), which is a material-specific constant that determines how much the resistance increases with temperature,
- T is the temperature in Celsius (or Kelvin, with appropriate conversions).

For the relationship between temperature and power, the power consumed by the filament is related to its temperature and follows a nonlinear relationship governed by the Stefan-Boltzmann law for radiative heat loss:

$$P = \varepsilon\sigma A T^4 \quad \text{Eq. 13}$$

Where:

- P is the power radiated by the filament,
- ε is the emissivity of the filament,
- σ is the Stefan-Boltzmann constant 5.67×10^{-8} W/m^2 K^4,
- A is the surface area of the filament,
- T is the absolute temperature in Kelvin.

3.3.2 Fabrication of the toroidal heater

After finalizing the design, the heater coil drawing was sent to SLRI's machine shop for fabrication, as shown in Figure 3.29. For the insulator between the ionizer body and the heater coil, alumina paste was selected, allowing it to be pressed into the body's grooves for effective insulation. To apply the paste, a tamper tool was 3D-printed at SUT QLAB, as shown in Figure 3.30. The application process was first tested using modeling clay as a stand-in for the alumina paste to ensure proper fit and handling.

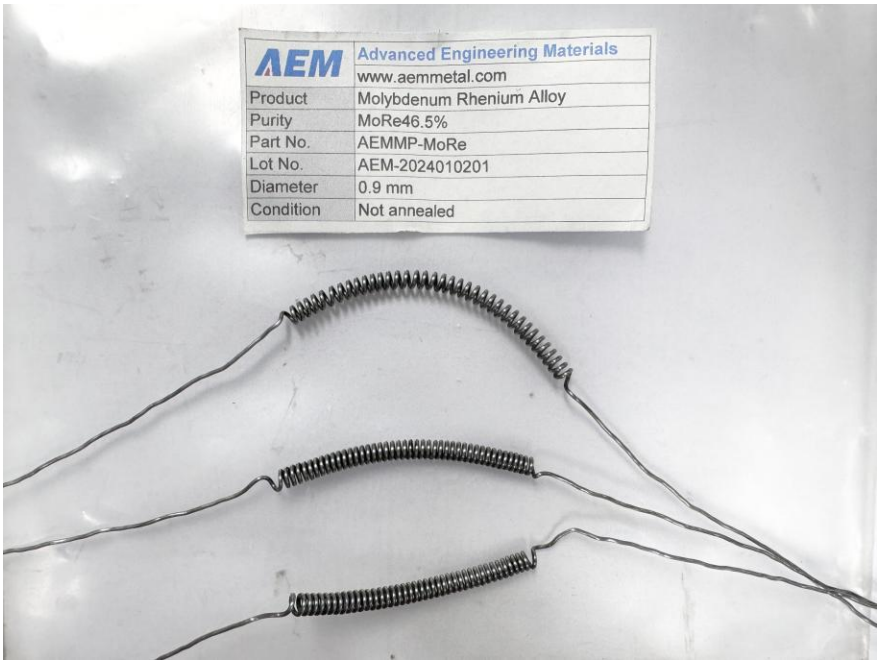

Figure 3.29 Fabrication of the toroidal heater coil by SLRI's machine shop.

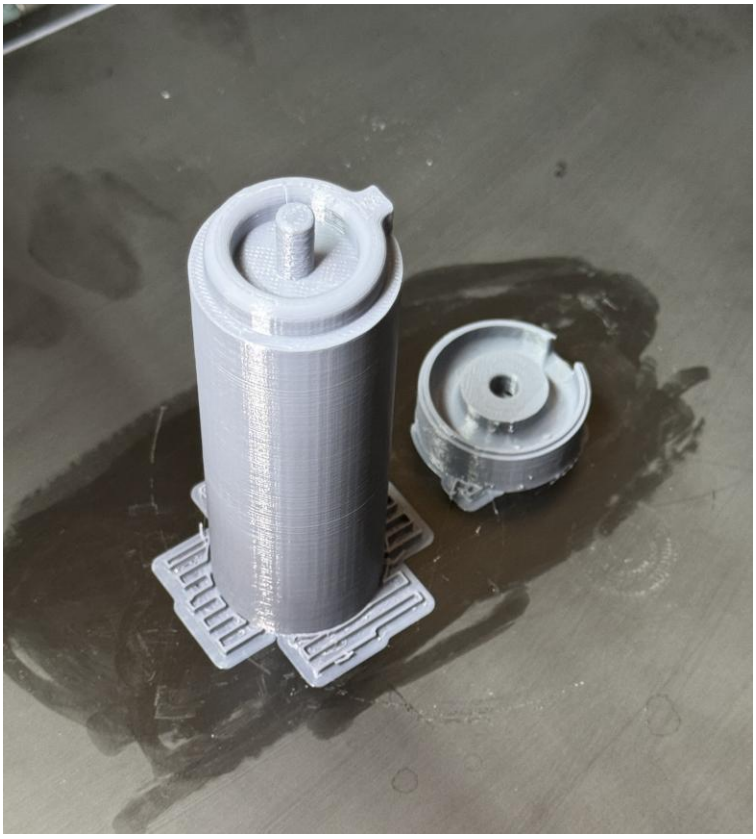

Figure 3.30 3D-printed prototype of the tamper by SUT QLAB.

3.3.3 Experimental setup

Once all preparations were complete, the heater coil test was set up under vacuum, as shown in Figure 3.31. An SLRI vacuum chamber was selected for its suitable ports, including a high-current feedthrough, flex hose, CF203 viewport, and pressure gauge. A pyrometer was used to measure the coil's temperature based on its thermal radiation, with an emissivity (**ε**) of 0.17 applied for MoRe and the pyrometer positioned 22 cm from the coil through the viewport, with video output displayed on a monitor. A mobile vacuum pumping unit—consisting of a scroll pump and a turbomolecular pump—was connected to the chamber via the flex hose. The high-current power supply was attached to the feedthrough using a custom connector that also secured the coil in place. Finally, the pressure gauge was installed on the chamber to monitor vacuum levels during testing.

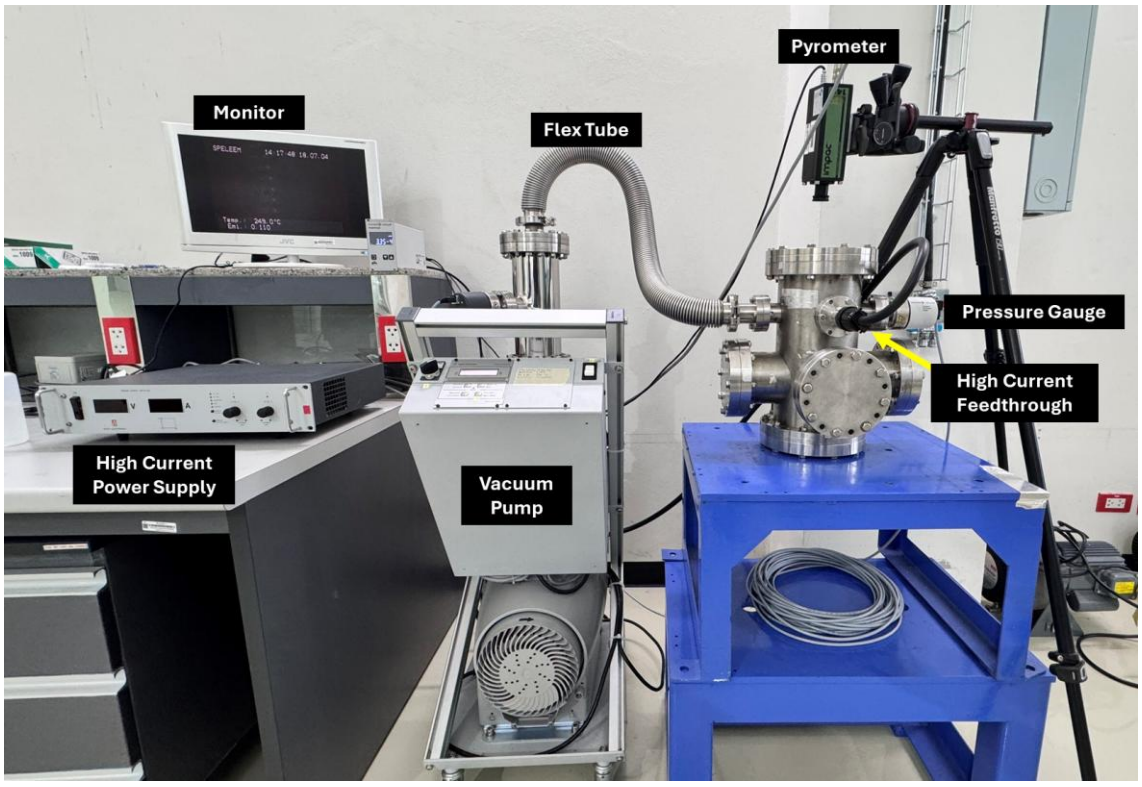

Figure 3.31 Experimental setup for heating the MoRe coil in the vacuum system.